WATER RESOURCES RESEARCH, VOL. 49, 2213–2227, doi:10.1002/wrcr.20210, 2013

Instantaneous turbulent forces and impulse on a rough bed: Implications for initiation of bed material movement

Ahmet Ozan Celik,[1] Panayiotis Diplas,[2] and Clint L. Dancey[3]

Received 10 January 2012; revised 18 March 2013; accepted 21 March 2013; published 26 April 2013.

[1] The overall objective of this study is to identify the physical mechanisms responsible for the entrainment of an exposed particle subject to rapidly fluctuating hydrodynamic forces in the case of channel flow with a fully rough boundary. This is pursued here by examining particle dislodgment under uniform and cylinder wake-flow experiments. The critical impulse concept is investigated more rigorously by measuring directly the pressures at four points on the surface of a fixed test grain. The number of impulse events determined from these experiments increases by more than an order of magnitude, over a modest change of roughness Reynolds number. Furthermore, they are well described by a log-normal probability density function. Both results are consistent with those obtained from similar experiments via indirect (velocity-based) impulse calculations and reported in a prior contribution. This comparison supports the use of the velocity record for determining instantaneous hydrodynamic forces and impulses instead of the more difficult approach of measuring the pressure fluctuations directly. The present results demonstrate the dominant role the local, streamwise velocity component plays on particle dislodgment. This is attributed to the large impulse content and occasionally strong positive lift force associated with flow events, exhibiting pronounced positive streamwise velocity fluctuations. The majority (~70%) of these events occur in the fourth quadrant, while a significant number (~22%) appear as first-quadrant episodes. It was also determined that wake flows can increase substantially particle entrainment via enhanced lift and increased turbulence intensity.

Citation: Celik, A. O., P. Diplas, and C. L. Dancey (2013), Instantaneous turbulent forces and impulse on a rough bed: Implications for initiation of bed material movement, *Water Resour. Res.*, *49*, 2213–2227, doi:10.1002/wrcr.20210.

1. Introduction

[2] The common perception in sediment transport research, especially for conditions near threshold of motion, is that the fluctuating drag and lift forces acting on individual grains due to turbulent flow are responsible for particle entrainment. Force or moment balances based on the magnitude of the fluctuating forces have been employed to establish the condition for threshold of movement in deterministic and probabilistic models [*Coleman*, 1967; *Wiberg and Smith*, 1987; *Papanicolaou et al*., 2002; *Wu and Chou*, 2003; *Smart and Habersack*, 2007, and references therein]. According to these approaches, near-bed extreme flow events exerting high magnitude instantaneous forces (above a critical value) on individual grains will always cause particle entrainment. This concept is perhaps best illustrated in *Grass* [1970] as the overlap between the probability distribution of the instantaneous turbulent stress and the distribution of critical stress for a sediment bed.

[3] Over the last several decades, this line of thinking has led many researchers to device experimental strategies in an effort to clarify the role of turbulent flow on particle entrainment. While *Sutherland* [1967] and *Jackson* [1976] initially pointed out the importance of flow structures on particle entrainment, *Heathershaw and Thorne* [1985] and *Nelson et al*. [1995] were among the first to experimentally establish the quantitative correlation between specific flow events and bedload transport. *Heathershaw and Thorne* [1985] examined the initiation of motion of sea-bed gravels in tidal flows. They used electromagnetic current meters to measure velocity fluctuations in the vertical and longitudinal directions, while an underwater video camera together with a wideband hydrophone were employed to monitor sediment movement. They concluded that most of the sediment movement was caused by sweep-type (Q IV) events and to a lesser extent by outward interactions (Q I). These results led them to suggest that streamwise velocity fluctuations have greater significance in terms of sediment transport. *Nelson et al*. [1995] obtained similar results from laboratory experiments carried out under fully developed channel flow conditions and for the case of a flow behind a

[1]Civil Engineering Department, Anadolu University, Eskisehir, Turkey.
[2]Baker Environmental Hydraulics Laboratory, Department of Civil and Environmental Engineering, Virginia Tech, Blacksburg, Virginia, USA.
[3]Baker Environmental Hydraulics Laboratory, Department of Mechanical Engineering, Virginia Tech, Blacksburg, Virginia, USA.

Corresponding author: P. Diplas, Baker Environmental Hydraulics Laboratory, Department of Civil and Environmental Engineering, Virginia Tech, Blacksburg, VA 24061, USA. (panos2007@gmail.com)

0043-1397/13/10.1002/wrcr.20210

backward-facing step. In both cases, they synchronized fluctuating bedload transport measurements with pointwise, two-component laser Doppler velocimeter (LDV) measurements in close proximity to the bed. Similarly, they demonstrated a strong correlation between the streamwise velocity (Q I and Q IV events) and bedload transport, with Q IV events predominating due to their frequency of occurrence.

[4] More recently, technological advancements have allowed for direct measurements of time-resolved forces (lift and drag) on an instrumented immobile grain [e.g., *Schmeeckle et al*., 2007; *Dwivedi et al*., 2011a, 2011b] or of time-resolved grain surface pressures [*Hofland et al*., 2005; *Smart and Habersack*, 2007; *Dwivedi et al*., 2010; *Detert et al*., 2010; *Celik*, 2011]. To capture the grain/flow interaction, the force or pressure measurements were synchronized with simultaneous time-resolved velocity measurements. *Hofland et al.* [2005] and *Dwivedi et al*. [2010, 2011a] report, in addition to pressure or force measurements, separate mobile grain experiments with simultaneously recorded particle image velocimetry (PIV) measurements. A number of other investigations report simple grain entrainment observations simultaneously with flow velocity (via either LDV or PIV) without providing separate force or pressure measurements, notably *Balakrishnan* [1997], *Cameron* [2006], and *Celik et al*. [2010].

[5] More specifically, *Detert et al*. [2010] measured bed surface pressure using an array of transducers mounted on the surface of a rough immobile bed together with simultaneous PIV measurements of the flow field. Their results show a decrease in the pressure on the top of the grains as higher velocity zones travel over the transducers. Higher pressures were observed during the passage of low-velocity fluid zones. Similar PIV measurements in a horizontal plane just above the roughness clearly showed high- and low-speed streaks, random but alternating in the spanwise direction.

[6] *Dwivedi et al*. [2011a] obtained PIV measurements in two separate sets of experiments, one with a mobile and the other with an immobile test grain, to examine the role of coherent flow structures on the initiation of grain entrainment under fully rough bed conditions. For the immobile tests, the instantaneous PIV velocity measurements are encoded with the hydrodynamic forces (drag and lift) applied on a single spherical grain, positioned among identical spheres, and measured simultaneously via the use of a force transducer. For the mobile grain tests, instantaneous PIV measurements are obtained together with grain entrainment (video) detection. Regardless of the degree of grain exposure, large sweep (Q IV) structures predominated during its entrainment. The authors concluded that strong sweeps induce high drag forces as well as high pressure below the grain, leading to positive lift. The simultaneous PIV/force measurements with the immobile grain revealed outward interaction (Q I) events preceding a sweep with maximum drag and lift observed during sweeps.

[7] In the present work, we extend the scope of the recent investigations on individual grain/flow interaction by emphasizing the role of impulse on the initiation of motion [*Diplas et al*., 2008]. According to this theory, the majority of high-magnitude turbulent flow events occurring immediately upstream of a grain are short lived and therefore ineffective for completely dislodging the grain from its initial position, even when they are well above a known critical value. Furthermore, turbulent events of not as high magnitude (still above a critical value) but lasting longer may be capable of dislodging the grain from its pocket. These conclusions, which were obtained from direct observations of the movement of a test grain together with synchronously measured near-bed flow velocity, suggest that the magnitude of fluctuating forces acting on individual grains, even its extreme values, is insufficient to unambiguously identify threshold conditions. In addition to magnitude, the duration over which a force acts needs to be considered. Thus, impulse, which accounts for both force magnitude, F, and duration, T, was proposed as the suitable parameter for determining the threshold of particle movement condition. This new criterion, initially proposed by *Diplas et al*. [2008], was validated both experimentally and analytically by the same authors. The existence of a critical impulse (rather than a critical force) implies that, theoretically, an infinite number of force magnitude (exceeding the critical level) and event duration combinations exist that can trigger entrainment of a grain as long as their product, the impulse, is above a critical value appropriate to the grain and its local bed geometry (its pocket). We note that during entrainment the unbalanced force acting on the grain may change with time (due to changing resistance and applied hydrodynamic force); however, the entrainment of a grain is still well captured by a critical value of the impulse, which accounts for the accumulated time integral of the varying unbalanced force. The existence of such a critical impulse as well as the wide range of combinations of force magnitude and duration that can cause entrainment have been demonstrated in *Diplas et al*. [2008], *Valyrakis et al*. [2010], and *Celik* [2011]. This assertion was independently validated later by the work of *Dwivedi et al*. [2011a, Figure 19].

[8] The present work examines the following issues as they relate to the initiation of motion of individual sediment grains within the context of the impulse concept: (1) due to the rapidly fluctuating nature of turbulent flow, the distribution of impulse imparted by the flow upon a grain represents the pertinent parameter for determining the probability of particle entrainment. Using an indirect method for estimating the instantaneous force record (from the velocity measurements obtained upstream of a test grain via LDV) and computing the associated impulse, *Celik et al*. [2010] proposed a log-normal distribution for the impulse parameter. The validity of this result is examined here by using direct measurements of the grain surface point pressures to determine impulse values. (2) It is well known that the rate of grain entrainment is extraordinarily sensitive to very modest changes in flow conditions (e.g., the mean bed shear stress) for near-threshold conditions [*Nelson et al*., 1995; *Sumer et al*., 2003; *Diplas et al*., 2010]. Here we investigate the characteristics of flow-induced force magnitudes during individual impulse events in order to determine the sensitivity of these forces to such modest changes in flow conditions. (3) To better understand the characteristics of impulse events (exceeding the critical value required for grain entrainment), the relationship between the force (lift and drag) magnitudes, their

temporal durations and flow velocities (and associated quadrant events) which contribute to them is examined.

[9] These issues are addressed through a series of experiments, including mobile grain experiments as well as measurements using an immobile instrumented grain and simultaneous flow-velocity measurements. Details of the experimental design and instrumentation are presented next, followed by a section on the detection of impulse and the presentation of the results. We conclude our results in section 5.

2. Experiments

[10] The overall objective of this study was to examine the physical interactions responsible for the entrainment of an exposed particle (referred to as a target grain as well) subject to turbulent fluid forces in the case of channel flow above a rough bed of spheres. For this purpose, we carried out two types of experiments: one under uniform flow conditions and the other in the presence of a submerged horizontal cylinder spanning across the channel upstream of the target grain (representing unsteady wake-flow conditions). For each type, we conducted both fixed and mobile particle experiments. In the fixed particle experiments, we obtained a continuous record of simultaneously measured pressure data on the surface of the target particle and the flow velocity one diameter upstream of it and along its centerline. In the other experiment, we employed a mobile grain and recorded the occurrence of its entrainment while simultaneously measuring the near-bed velocity, again one grain diameter upstream and along its centerline. A tilting flume 14.4 m long and 0.6 m wide with a fixed slope of 0.25% was used for all of the experiments. The flume test section used in all experiment series was identical and consisted of a 12.7 mm diameter, d, spherical grain resting on two layers of well-packed identical spheres, as shown in Figure 1. This simplified bed geometry was selected to reduce the complexities associated with the variations in the bed and flow details and therefore make it easier to identify the nature of the flow characteristics responsible for grain entrainment. The majority of the flume tests were performed in fully developed uniform open-channel flow at near-threshold conditions (Shields parameter ~ 0.01) for a range of roughness Reynolds numbers ($Re^* = u^* d/\nu$, where u^* is the friction velocity and ν is the kinematic viscosity) (Table 1). Similar pressure and particle entrainment experiments were performed in the wake of a cylinder (see Figure 1b for cylinder wake test configuration).

[11] In the mobile particle experiments, entrainment of a Teflon® grain was recorded utilizing a separate laser-based system that detects its initial movement, continuous displacement, and its full dislodgment [*Diplas et al.*, 2010]. This nonintrusive technique is based upon laser illumination of the test grain and the modulation of the received light intensity due to the movement of the target grain. The output from this system is recorded simultaneously with the measured flow velocity for postprocessing. For the fixed grain experiments, a spherical particle, identical in size to the mobile one, was instrumented with four low-range pressure transducers and was securely attached to the flume bed, to measure the instantaneous surface pressures simultaneously at its front (p_1), back (p_2), top (p_3), and bottom (p_4) as shown in Figure 1a. Differences between

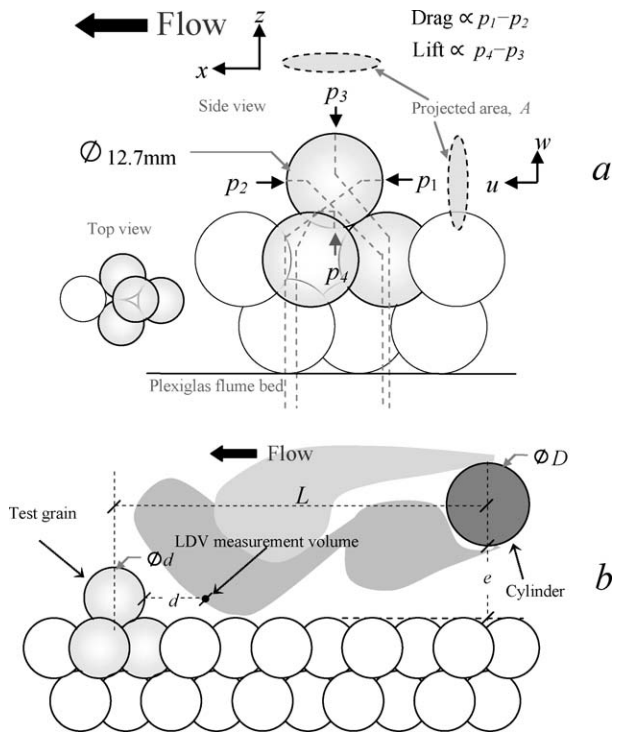

Figure 1. Bed configuration of mobile and instrumented particle experiments. (a) Definition sketch for the pressure measurement points and bed geometry. (b) Side view of the test section with the test particle in the wake of a cylinder.

these simultaneously measured separate pressure signals were used to estimate the corresponding forces (drag and lift) on the grain.

[12] The instrumented immobile sphere used for the surface pressure measurements was an in-house custom designed fixture attached to the flume bed and mounted on top of three identical size spheres arranged in a hexagonal packed structure consistent with the surrounding bed grains (Figure 1). The ports used for measuring the pressures at the four selected sites on the grain surface were 1 mm in diameter. Each port was individually connected via brass tubing mounted interior to the spherical grain and passing through the base grains through the bottom of the flume to separate Honeywell, Sensotec FP-2000 series pressure transducers. The manufacturer's specifications report flat frequency response to 300 Hz, a full-scale range of 25.4 cm of water column at 5 V output with 0.1% accuracy from the best fit straight line for the operating temperature of the tests. The analog voltage output from the transducers was digitally sampled with 16 bit resolution with a separate data acquisition system, yielding a final resolution of 0.076 mV (0.038 Pa). The pressure transducers were statically calibrated in a plexiglass calibration box. This calibration yielded a linear response for all transducers. The highest standard error of the estimate from the regression analysis on the calibration data was 1.05 Pa, which represents approximately 1% of the pressure difference required to overcome the submerged weight of a Teflon grain of 12.7 mm diameter.

[13] In addition to the static calibration, a dynamic characterization of the transducers was performed. The calibration

box was outfitted with a 25.4 cm diameter subwoofer to generate a fluctuating pressure field in the box with the separate transducers mounted in the instrumented grain and under 3.8 cm of water. Transducer 3 (the top of the grain) was used as the control and the response of the transducers to white noise was sampled at 1 kHz. The purpose of these dynamic characterization tests was to determine whether the tubing used to connect the pressure ports in the sphere surface to the transducers below the flume affected the transducer response. The transfer function between the control transducer and the others revealed the tubing effect to be negligible up to 100 Hz. All pressure signals were filtered at 90 Hz for the measurements reported here.

[14] In all experiments, the mobile and instrumented grains were placed on the centerline of the flume bed and the instantaneous fluid velocity components, u and w, in the streamwise and vertical directions, respectively, were measured one particle diameter upstream of the mobile/instrumented grain along its centerline via a two-component LDV. For more details, see *Celik et al*. [2010]. The sampling duration for each flow condition in all experiments was 15 min with an average data rate of 250 Hz. A right-handed Cartesian coordinate system (x, y, z), where x is streamwise along the flume axis, y is spanwise across the flume, and z is perpendicular to the flume bottom was adopted in this study.

[15] The second set of experiments with both mobile and immobile grain measurements were performed with a circular cylinder mounted upstream of the target grain and horizontally across the width of the channel. It is well known that the wake flow downstream of a bluff body is characterized by higher turbulence intensities and larger pressure fluctuations acting on the wall. In many practical river engineering applications, flow is altered due to the presence of bedforms and hydraulic structures. These conditions lead to a significant increase in sediment movement and result in scour near these hydraulic structures in rivers and waterways [*Sumer et al*., 2003; *Radspinner et al*., 2010]. The purpose of the wake-flow tests was to examine the way in which the presence of a cylinder and the flow structures induced by it, and accompanied lift force [see *Celik*, 2011] influence the impulse imparted to an exposed grain in its wake, and its resulting entrainment rate.

[16] For the wake studies, four different size PVC pipes, with diameters (D) of 3.34, 2.67, 2.19, and 1.27 cm, were used. Figure 1b illustrates the bed conditions with the cylinder. L and e in Figure 1b are the distance between the center of the instrumented test grain and centerline of the cylinder in the streamwise direction, and the distance between the bed (top of the spheres in the uppermost layer) and the bottom of the cylinder, respectively. L was chosen to be $2.5D + 1.5d$, as this location was where the highest turbulence intensity (obtained from near-bed velocity measurements) was measured in preliminary flume tests. e was set equal to D, so that $e/D = 1$ to avoid suppression of the vortex shedding due to rough bed proximity [*Sumer and Fredsøe*, 2006].

[17] A summary of the flow conditions for all the flume tests is given in Table 1. A total of 10 uniform flow conditions were tested. The UC experiment was used as the basis for performing the four different cylinder diameter tests. That is, it represents the undisturbed, uniform, and fully developed turbulent channel flow before a test cylinder is placed in the flow field. Both fixed and mobile particle experiments were performed for each of the following cases: U2–U8, UC, and CD1–CD4 [*Celik*, 2011]. However, in the present work, for the uniform flow experiments, we concentrate only on the fixed grain tests, and for the wake flows, we consider both fixed and mobile grain results.

3. Impulse Detection

[18] The emphasis of this investigation is on flow impulse as a mechanism for initiating grain entrainment (as detailed in *Diplas et al*. [2008]; *Valyrakis et al*. [2010], and *Celik* [2011]). Impulse is defined by $I = \int_{t_1}^{t_2} F\mathrm{d}t$ where F is the applied force and $T = t_2 - t_1$ is the duration of the force. The force magnitude, F, applied to the grain over an interval T are the two contributing factors to impulse. In the fixed, instrumented grain experiments the magnitudes of

Table 1. Summary of Flow Conditions

Run	Depth average velocity, U (cm/s)	Flow depth, h (cm)	Re^*	Pressure measurements	TI	Particle entrainment tests	Particle entrainment frequency, n_e (Ent./min)	I_{mean} (Ns)	I_{std} (Ns)	C_D	mean	u^* (m/s)
U1	47	8.1	438	Yes	0.28	No		0.0006	0.0007	1.292	1.731	0.0345
U2	45	7.5	424	Yes	0.27	Yes	6.93	0.0004	0.0004	1.287	1.690	0.0334
U3	43	8.2	413	Yes	0.27	Yes	5.73	0.0004	0.0003	1.198	1.659	0.0325
U4	41	7.9	398	Yes	0.27	Yes	2.06	0.0004	0.0003	1.170	1.592	0.0313
U5	42	8.3	385	Yes	0.27	Yes	1.33	0.0003	0.0002	1.023	1.492	0.0303
U6	40	8.6	377	Yes	0.26	Yes	0.52	0.0003	0.0002	1.026	1.496	0.0297
U7	41	9.1	372	Yes	0.26	Yes	0.24	0.0003	0.0003	1.017	1.476	0.0293
U8	39	8.7	364	Yes	0.27	Yes	0.14	0.0002	0.0002	0.881	1.452	0.0287
U9	35	8.9	330	Yes	0.26	No		0.0002	0.00012	0.818	1.334	0.0260
UC	43	9	399	Yes	0.27	Yes	4.2	0.0004	0.0004			0.0314
	Cylinder Diameter (cm)											
CD1	3.34			Yes	0.36	Yes	19.8					
CD2	2.67			Yes	0.41	Yes	22					
CD3	2.19			Yes	0.43	Yes	25.4					
CD4	1.27			Yes	0.31	Yes	6.6					

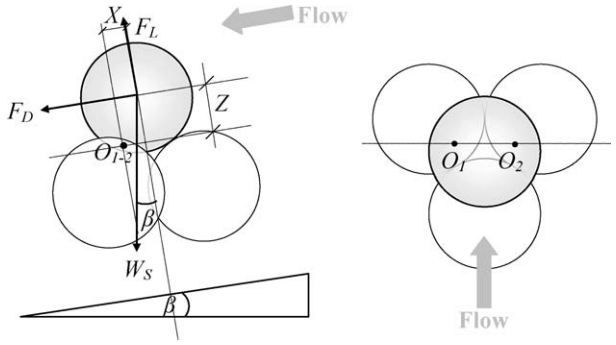

Figure 2. Definition sketch of the forces acting on a spherical particle resting on identical size densely packed spheres: (left) side view and (right) top view of the bed geometry. This is the arrangement that was used for both the pressure and the particle entrainment measurements.

the instantaneous forces were estimated from the measured instantaneous pressure differences using $F_D = A(p_1 - p_2)$ and $F_L = A(p_4 - p_3)$, where F_D is the estimated drag force, F_L is the lift force and A is the area of the spherical test grain projected in both horizontal and vertical planes [*Einstein and El-Samni*, 1949; *Hofland et al*., 2005; see the definition sketch and the insets in Figure 1a]. For the analysis hereafter, we consider F_L as the effective lift force that excludes the buoyancy force acting on the submerged 12.7 mm diameter grain. The pressure distribution on the surface of the sphere is expected to be nonuniform and dynamic, so our estimates of force from the stagnation pressure, base (leeward side) pressure, and the pressures on the top and bottom are expected to yield forces somewhat in excess of the true instantaneous pressure forces. The procedure to detect the impulse events is explained below.

[19] The forces acting on the mobile particle for the given grain configuration (Figure 2) are submerged particle weight, W_S, F_D, and F_L, all assumed to act through the center of gravity of the sphere [*White*, 1940; *Gessler*, 1971]. For all of the uniform flow experiments, the Shields parameter is approximately 0.01, which is consistent with the incipient condition for a fully exposed sediment grain [*Fenton and Abbott*, 1977]. Physically, the test grain is highly exposed to the flow (82% exposure), and the drag force, F_D, is the prevailing hydrodynamic force component, and the preferred mode of particle entrainment is rolling for these near threshold of motion conditions [*Sutherland*, 1967; *Fenton and Abbot*, 1977; *Diplas et al*., 2008]. Turbulence fluctuations in the F_D time series, which are above the minimum (critical) drag force necessary for particle movement, $F_{D\mathrm{cr}}$, are treated as impulses (equation (2) below). $F_{D\mathrm{cr}}$ can be obtained from a moment balance:

$$F_{D\mathrm{cr}} = \frac{X}{Z}(f_v W_s \cos(\beta) - F_{L\mathrm{mean}}) - f_v W_s \sin(\beta), \qquad (1)$$

where f_V is the hydrodynamic mass coefficient [*Papanicolaou et al*., 2002], $f_V = (1+0.5(\rho/\rho_S - \rho))$, ρ is the density of water, ρ_S is the density of the Teflon particle (2300 kg/m^3), X and Z are the lever arms obtained from the bed geometry, aligned with the bed and normal to the bed, respectively, and β is the angle between the channel bed and the horizontal plane (Figure 2). Though it is generally assumed that the drag dominates grain dislodgment for highly exposed particles, the time-averaged lift force over the entire sampling duration, $F_{L\mathrm{mean}}$, is included in equation (1) contributing to an effective particle weight, as previously proposed by *Zanke* [2003].

[20] From the time history of drag force acting upon a particle $F_D(t)$, the impulse, I, can be calculated as follows:

$$I = \int_{t_1}^{t_2} F_D(t)\mathrm{d}t = < F_D > T \quad \text{with} \quad F_D(t) \geq F_{D\mathrm{cr}} \ \text{between} \ t_1 \ \text{and} \ t_2, \qquad (2)$$

where $T = t_2 - t_1$ is the duration of the applied force, $\langle F_D \rangle$ is the time-average drag force over duration T (angle brackets denote time averaging over the duration of the impulse event, T). It is understood that such impulse events occur intermittently and randomly, whenever the applied force exceeds the critical force. The duration over which $F_D \geq F_{D\mathrm{cr}}$ during the ith event, T_i, is illustrated in Figure 3a. The time-average F_D value, $\langle F_D \rangle_i$, representative of the average drag force of the ith event with $F_D \geq F_{D\mathrm{cr}}$ and impulse magnitude, $I_i = \langle F_D \rangle_i T_i$, can be determined from the data series in postprocessing. In addition, time-average F_L value, $\langle F_L \rangle_i$, representative of the average lift force acting on the grain for the period of T_i of the ith event can be computed for all events (Figure 3b). Simultaneously measured near-bed flow velocity components u and w are also shown in Figures 3c and 3d, respectively. In order to account for the phase delay between the flow velocity and force signals due to the distance between the grain and the location of the LDV measurement volume, the flow velocity records were shifted forward by the lag time obtained at the maximum of the cross-correlation function between u and p_1 [*Celik*, 2011]. In this way, the near-bed flow events and the forces they generate on the particle were matched in time before the impulse analysis was performed. The procedure described here was implemented and the series of random impulse events (and associated I_i, T_i, $\langle F_D \rangle_i$, $\langle F_L \rangle_i$, $\langle u \rangle_i$, and $\langle w \rangle_i$) for each run were detected. The following section elaborates on the properties of the impulses and their relation to the flow parameters.

4. Results

[21] For the results presented here, we focus exclusively on those flow events for which $F_D > F_{D\mathrm{cr}}$. That is, only on those events for which the drag force on the grain exceeds the critical value and flow impulse is generated. Averages apply to these individual events and ensembles of these events. We note, however, that in determining $F_{D\mathrm{cr}}$ (equation (1)) the conventional time mean average over the full time series of the lift force, F_L, is used.

4.1. Distribution of Directly Detected Impulse Events With $F_D \geq F_{D\mathrm{cr}}$

[22] Both histograms of event duration and impulse values obtained from the measured pressures acting on the test grain and associated with events satisfying $F_D \geq F_{D\mathrm{cr}}$, are

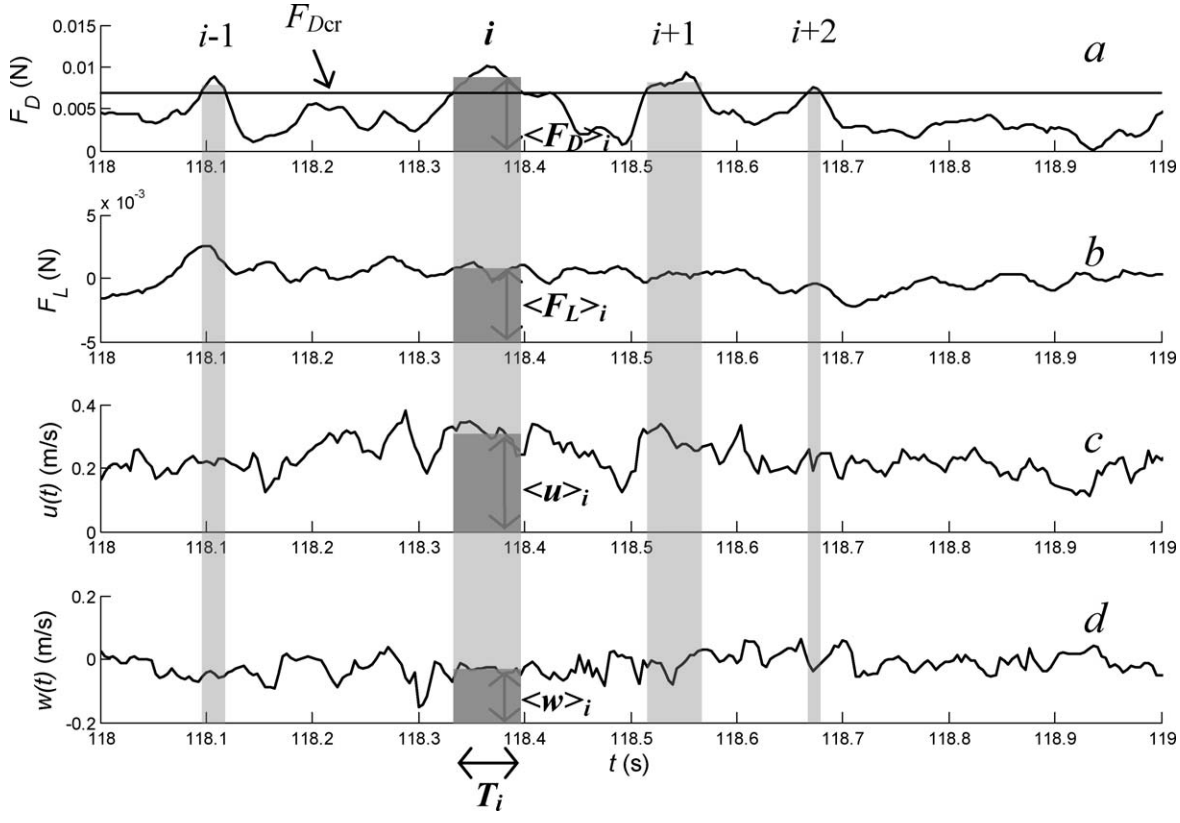

Figure 3. Synchronized plot of measured forces acting on the test grain and flow velocities measured one diameter upstream of the grain. Representative time series of (a) F_D, (b) F_L, (c) u, and (d) w from run U3. Shaded vertical regions indicate events within F_D, F_L, u, and w time series during which $F_D \geq F_{D\mathrm{cr}}$. The ith event was selected to show the magnitude of $\langle F_D \rangle_i$, $\langle F_L \rangle_i$, $\langle u \rangle_i$, and $\langle w \rangle_i$.

positively skewed with a long tail (Figures 4a and 4b, respectively; data from run U2). These histograms are representative of all uniform flow test cases.

[23] Impulse values obtained indirectly from the $u^2(t)$ time series (i.e., $F_D(t) \sim \frac{1}{2}\rho u^2(t)$), associated with events satisfying $u^2 > u_{\mathrm{cr}}^2$, were found by *Celik et al*. [2010] to follow closely a log-normal distribution. By nondimensionalizing the random impulse variable, I, with its ensemble average value, I_{mean}, as $\hat{I} = I/I_{\mathrm{mean}}$, *Celik et al*. [2010] determined that the following log-normal expression

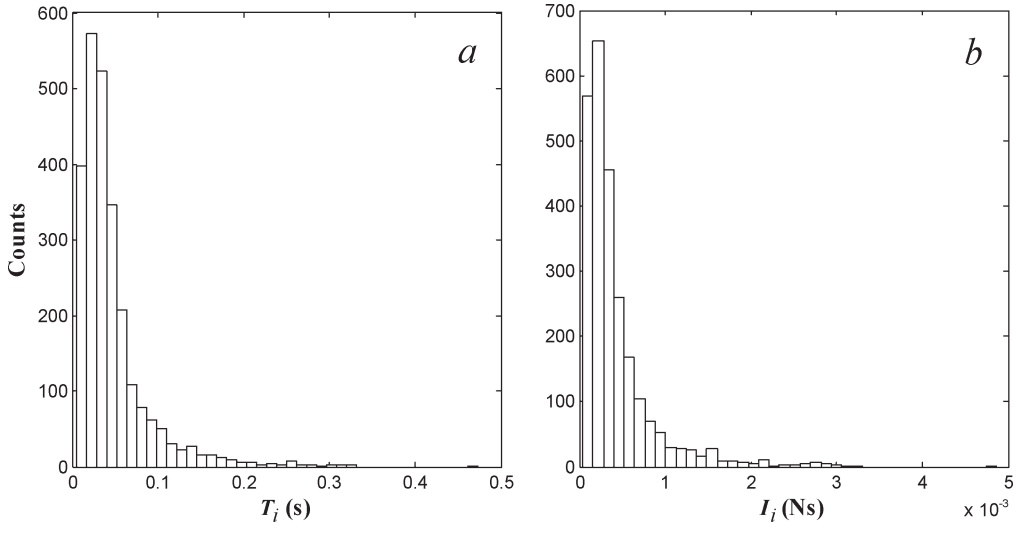

Figure 4. Histograms of the (a) event duration and (b) impulse. Data from run U2 are presented here.

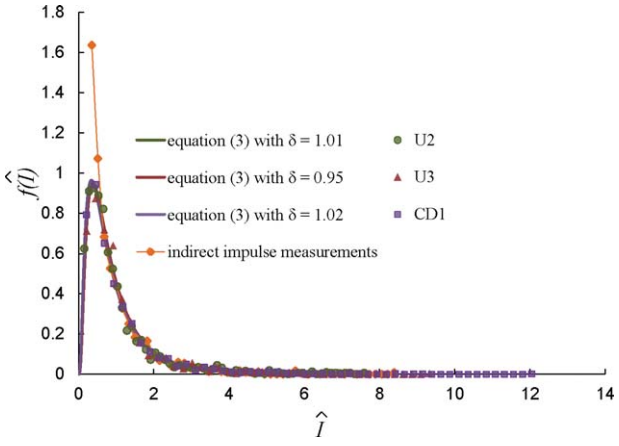

Figure 5. Comparison of equation (3) with measured pdfs for runs U2, U3, and CD1 (P values = 0.53, 0.65 and 0.56, respectively). Note that different δ values were used in equation (3) for each run. These δ values were determined from the corresponding data sets. Solid diamonds with orange color represent indirect impulse measurements (using $C_D = 0.9$ and accounting for the effect of time-averaged lift when calculating F_{Dcr} from equation (1)).

represents the corresponding probability density function (pdf) well,

$$f(\hat{I}) = \frac{1}{\sqrt{2\pi \ln(1+\delta^2)}\hat{I}} \exp\left[-\frac{\left(\ln \hat{I} + \ln\sqrt{1+\delta^2}\right)^2}{2\ln(1+\delta^2)} \right], \quad (3)$$

where $\delta = I_{\text{std}}/I_{\text{mean}}$ is the impulse intensity (coefficient of variation of impulse) and I_{std} the standard deviation of I.

[24] In an effort to test the validity of equation (3) in a more rigorous way, the pdf of directly measured (via the pressure taps) impulses from the F_D time series (with $F_D \geq F_{Dcr}$; for example, see Figure 3) are used here. Sample results are provided in Figure 5 for uniform runs U2, U3, and the unsteady wake case CD1. It is evident that the pdfs for all three runs are nearly identical and that equation (3) with the properly selected δ values (1.01, 0.95, and 1.02, respectively) follows the corresponding data very closely. For the U2 run, the impulse data calculated indirectly from the velocity record (with $C_D = 0.9$ and considering the effect of event-averaged lift force when determining F_{Dcr} from equation (1)), and the resulting pdf, have been included in Figure 5 for comparison purposes. This velocity-based procedure is described more extensively in *Celik et al*. [2010]. It appears that the direct method is more sensitive in detecting impulse events at or near the rising leg of the pdf. The present results demonstrate the suitability of a log-normal distribution (equation (3)) (or a similar long-tailed distribution, as discussed in *Valyrakis et al*. [2011]) for describing the pdf of the dimensionless impulse for both uniform and unsteady wake-flow conditions (Figure 5), as it was originally proposed by *Celik et al*. [2010] based on indirect measurements of the hydrodynamic forces.

4.2. Forces ($F_D \geq F_{Dcr}$) During Impulse Events

[25] Even though impulse rather than force magnitude is the relevant parameter for particle dislodgment under rapidly fluctuating hydrodynamic forces, here we investigate the relation between force magnitudes and the near-bed flow velocities encountered during the occurrence of impulse events. Such information is of paramount importance as the indirect approach constitutes the only practical way for determining the hydrodynamic forces applied upon an object in nearly all engineering/geomorphological applications.

4.2.1. Drag Coefficients of Impulse Events

[26] The drag coefficient averaged over the ith turbulent/impulse event, $\langle C_D \rangle_i$, is relevant to the impulse framework. Its value is calculated here from:

$$\langle C_D \rangle_i = \frac{2\langle F_D \rangle_i}{\rho A \langle u \rangle_i^2}. \quad (4)$$

[27] Here, $\langle u \rangle_i$ and $\langle F_D \rangle_i$ are the averaged velocity, u, and drag force, F_D (calculated from the measured surface pressures, $p_1 - p_2$), values determined over the duration of an impulse event, T_i, as shown in Figures 3a and 3c. The individual $\langle C_D \rangle_i$ values obtained from our experiments vary more than an order of magnitude within each run. As an example, the histogram of $\langle C_D \rangle_i$ values from run U2 is shown in Figure 6. This trend is representative of all uniform flow runs. The relationship between the $\langle u \rangle_i$ and $\langle C_D \rangle_i$ values is shown in Figure 7, where $\langle u \rangle_i$ has been nondimensionalized with the ensemble average of $\langle u \rangle_i$ values, $\langle u \rangle_{\text{mean}}$, determined for each of the experimental runs. The observed behavior follows the trends exhibited by the instantaneous drag coefficient values obtained by *Schmeeckle et al*. [2007] in their experiments. $\langle C_D \rangle_i$ varies inversely with $\langle u \rangle_i^2$ over a relatively wide range. It is noted that there are flow events with low near-bed velocities ($\langle u \rangle_i / \langle u \rangle_{\text{mean}} < 0.75$) exhibiting considerable increase in $_i$ with decreasing $\langle u \rangle_i$, thus resulting in high magnitude forces. Consequently, if the near-bed velocity is used together with a constant C_D value (a common consideration), then the calculated drag force magnitude and resulting particle movement estimated during these events will be significantly underestimated. Furthermore, for events with higher velocities ($\langle u \rangle_i / \langle u \rangle_{\text{mean}} > 1.25$), $\langle C_D \rangle_i$ values are nearly constant and typically below the ensemble average $\langle C_D \rangle_{\text{mean}}$. Although use of a constant drag coefficient will be appropriate in this case, the choice of $\langle C_D \rangle_{\text{mean}}$ will cause overestimation of the force magnitude and associated grain movement. Although more research is necessary, we adduce that the wide variation in the drag coefficient is largely due to the dynamic nature of the surface pressure field as flow structures of comparable size to the grain are advected downstream, inducing varying time lags between the upstream stagnation pressure and the downstream base pressure (directly on the back of the grain) [*Celik*, 2011].

[28] Since the impact of the near-bed extreme flow events on particle movement is better characterized by their impulse magnitude, I_i, [*Diplas et al*., 2008], it is important

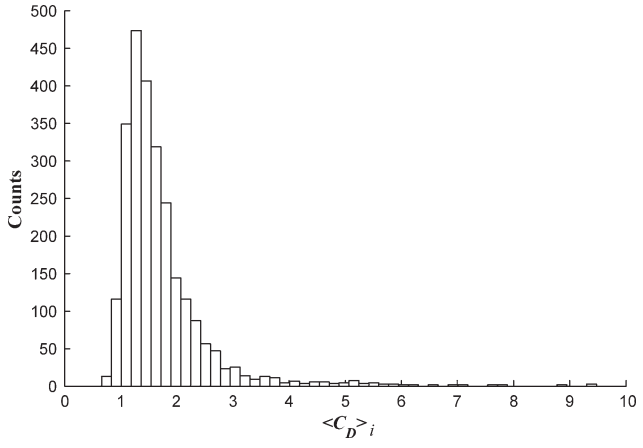

Figure 6. Histogram of the $\langle C_D \rangle$, 2522 data points from run U2 were used.

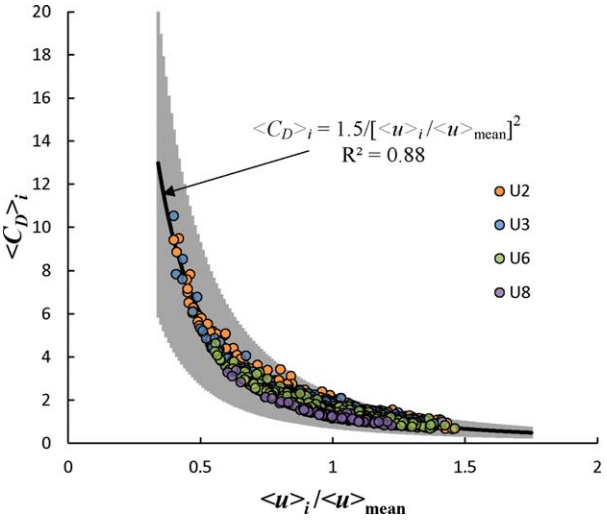

Figure 7. Scatterplot of $\langle C_D \rangle_i$. versus nondimensionalized $\langle u \rangle_i$. Shaded gray region represents ±50 variation in the drag coefficient magnitude about the best fit curve.

to establish the coupling of $\langle u \rangle_i$-$\langle C_D \rangle_i$ pairs with the corresponding event-based I_i values. This is shown in Figure 8 with a 3-D surface plot of $\langle u \rangle_i$, $\langle C_D \rangle_i$, and I_i (data from run U3). The extreme impulse events are generally observed in the high-velocity region ($\langle u \rangle_i > 0.9\ \langle u \rangle_{\text{mean}}$), where the variability in $\langle C_D \rangle_i$ values is small (Figure 7). Thus, the vast majority of the events with very high $\langle C_D \rangle_i$ values (>3), observed at low $\langle u \rangle_i$ in Figure 8, are not associated with impulse events that have the potential to dislodge a grain from its pocket. A similar plot of the lift forces, $\langle F_L \rangle_i$, encountered during these impulse events (Figure 9) does not provide any well-defined trends with $\langle C_D \rangle_i$ values. Both extreme negative and positive lift force magnitudes occur during events with lower $\langle C_D \rangle_i$ values (Figure 9). In Figure 9, the level of $\langle F_L \rangle_{\text{mean}}$ is explicitly shown, and, for clarity, lines representing ±2 standard deviations, $\langle F_L \rangle_{\text{std}}$, are also indicated. Further results on lift force characteristics, which will be presented in the subsequent sections, will be used to clarify its role on particle dislodgment.

4.2.2. Force and Related Impulse Event Histograms

[29] Representative histograms of the directly measured event-based force component magnitudes are presented in Figure 10 (data: run U2). The histogram of $\langle F_D \rangle_i$ (nondimensionalized by $F_{D\text{cr}}$) bears resemblance to a triangular (beta) distribution (Figure 10a). The distribution of $\langle F_L \rangle_i$ (nondimensionalized by W_s) is nearly Gaussian (Figure 10b). The same general distribution characteristics are observed for all runs under uniform flow conditions. As shown in Figure 10b, $\langle F_L \rangle_i$ can attain values up to ±20% of W_S for this flow condition. Values up to ±30% of W_S were obtained in other runs under uniform flow conditions. Such extreme positive lift forces will contribute to the particle dislodgment, while corresponding negative ones will have a stabilizing effect.

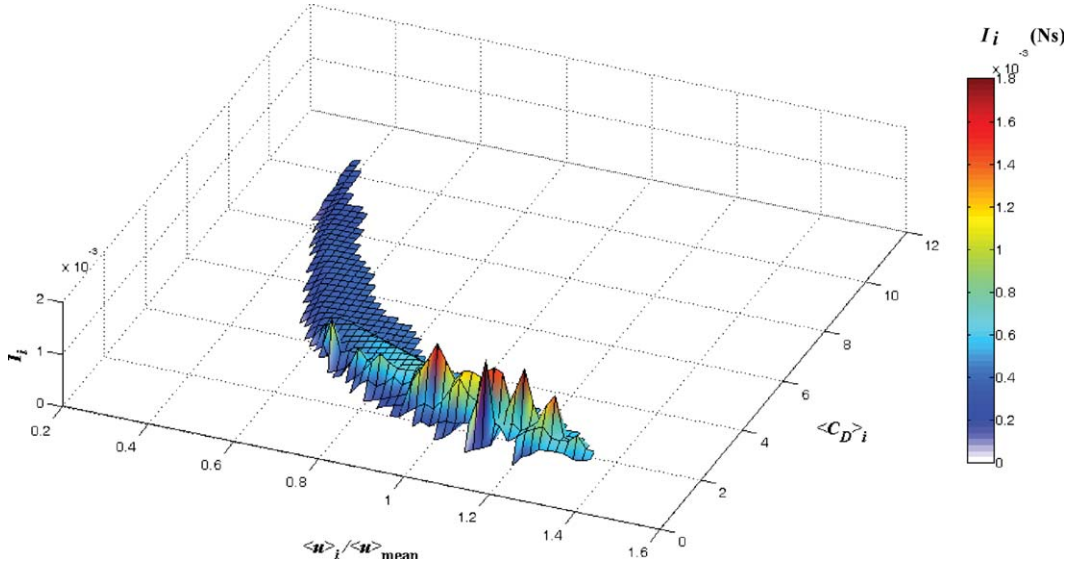

Figure 8. The 3-D surface plot of $\langle u \rangle_i$, $\langle C_D \rangle_i$, and I_i (data: run U3). Color bar indicates the impulse magnitude.

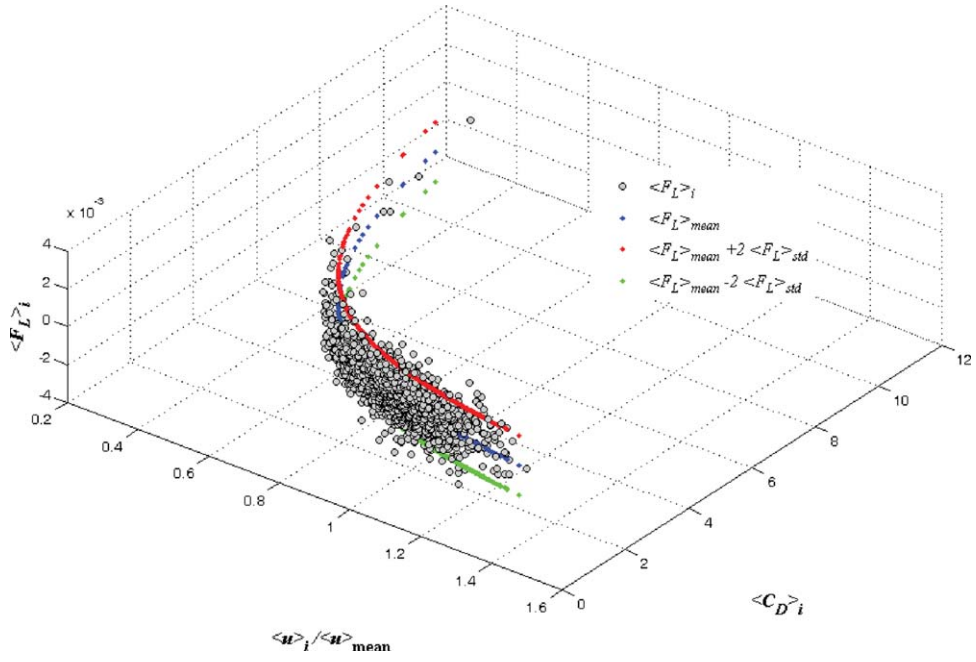

Figure 9. The 3-D scatterplot of $\langle u\rangle_i$, $\langle C_D\rangle_i$, and $\langle F_L\rangle_i$ (data: run U3). Blue ($\langle F_L\rangle_{\text{mean}}$), red, and green lines ($\langle F_L\rangle_{\text{mean}} \pm 2\langle F_L\rangle_{\text{std}}$) are obtained using the equation given in Figure 7 inset.

[30] The joint (2-D) histograms of $\langle F_D\rangle_i$ with $\langle F_L\rangle_i$ and I_i with $\langle F_L\rangle_i$ are shown in Figures 11a and 11b, respectively. A consistent tendency in the lift force direction (upward or downward) and magnitude with respect to the drag force and impulse trends is not apparent for low drag force and impulse values (e.g., see circled areas in Figure 11b). However, the majority of the lift forces coincident with higher drag (>0.11 N) and impulse (>1.5 N s) values are positive, and a significant number of them are of high magnitude. These results indicate that the lift force encountered during extreme impulse events is more likely to have a destabilizing effect on particle mobility.

4.2.3. Impulse Events and Quadrant Characterization

[31] In the previous sections, the forces and durations of flow events, where the force exceeds the critical value (impulse events), were examined. From these results, it is observed that the dimensionless drag force imparted by such impulse events varies modestly, above tens of percent (Figure 10a), while the temporal duration of these events

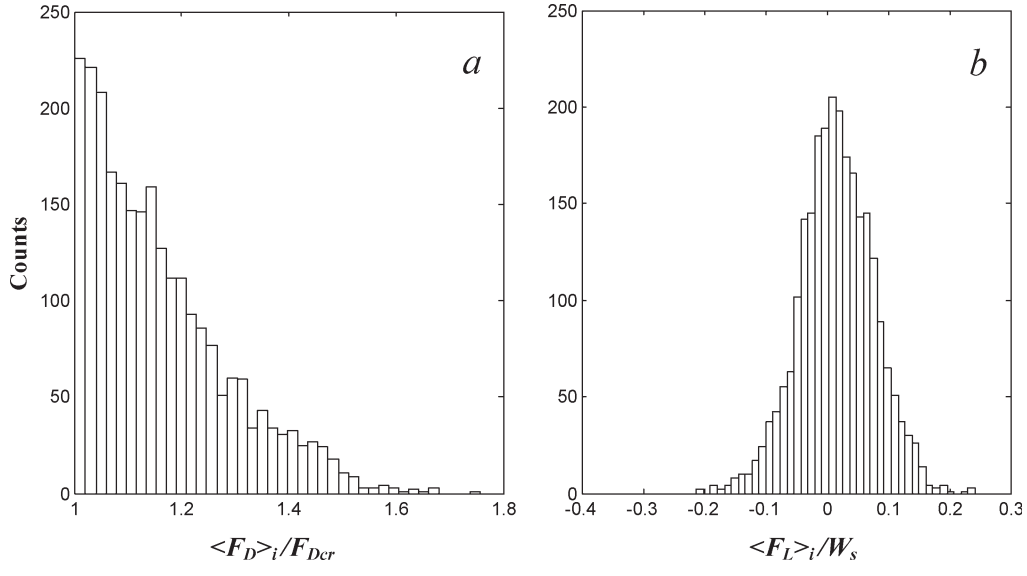

Figure 10. Histograms of the (left) event average drag force and (right) lift force. Data from run U2 are presented.

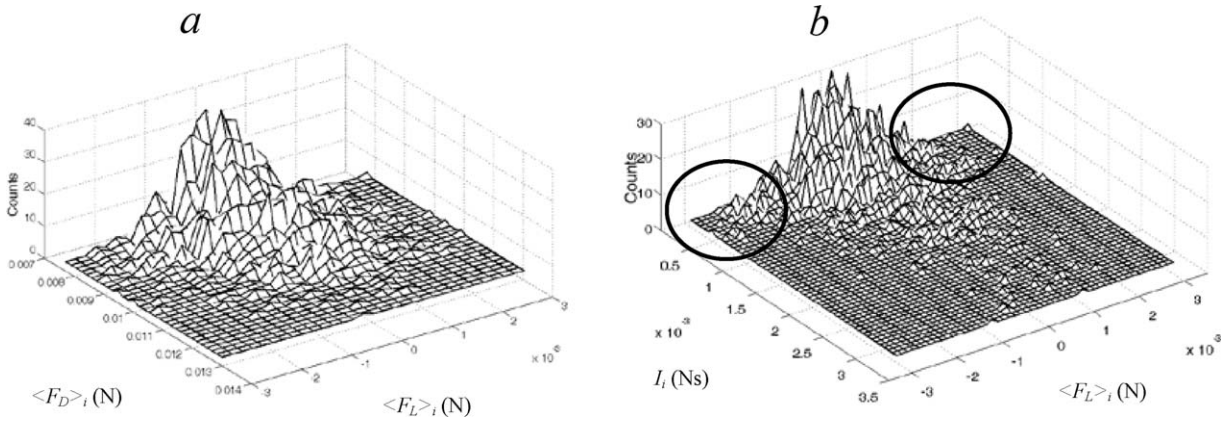

Figure 11. The 3-D mesh plot of the joint histogram of (a) drag force versus lift force and (b) impulse versus lift force (data from run U2–2522 data points were used, number of bins: 30×30 on -$\langle L \rangle$ plane and 50×50 on I-$\langle L \rangle$ plane).

varies by more than 1 order of magnitude (Figure 4a). This implies that the temporal characteristics of turbulent flow are extremely relevant for the entrainment of sediment. In this section, we examine the impulse, I_i, carried by these events and the lift force associated with them by using a variation of the conventional quadrant map. The goal is to ascertain the extent to which impulse events capable of moving the grain are associated with specific flow movements; and whether the lift imparted by the impulse event is relevant.

[32] Coherent structures in open-channel flow over rough beds have been studied extensively in sediment transport research. Recently, experimental studies of *Hofland et al*. [2005] and *Dwivedi et al*. [2010] using conventional quadrant analysis estimated the contributions from the four quadrants to the pressures acting on bed material and pointed out the importance of Q IV flow events. We note however that prior work by *Heathershaw and Thorne* [1985] and later by *Nelson et al*. [1995] demonstrated quantitatively that Q I events are equally effective, compared to Q IV, in moving sediment. The conclusion being that (1) the predominance of Q IV is due to their frequency not their effectiveness and (2) that streamwise velocity fluctuations are most relevant to grain entrainment. Since extreme impulse events are so closely tied to entrainment, here we consider the distribution of impulse magnitude on the $\langle u \rangle'$-$\langle w \rangle'$ plane, where we modify the usual Reynolds decomposition to identify the average velocity associated with each impulse event relative to the conventional mean value for the entire time series of the flow. That is, $\langle u \rangle_i' = \langle u \rangle_i - u_{\text{mean}}$ and $\langle w \rangle_i' = \langle w \rangle_i - w_{\text{mean}}$, where u_{mean} and w_{mean} are the average u and w values over the entire time series of each 15 min long experimental run (see Figure 3 for the description of $\langle w \rangle_i$ magnitude). Accordingly, the four quadrant regions can be defined as

$\langle u \rangle_i' > 0$ and $\langle w \rangle_i' > 0$, (Q I)
$\langle u \rangle_i' < 0$ and $\langle w \rangle_i' > 0$, (Q II)
$\langle u \rangle_i' < 0$ and $\langle w \rangle_i' < 0$, (Q III)
$\langle u \rangle_i' > 0$ and $\langle w \rangle_i' < 0$. (Q IV)

[33] This classification characterizes the four types of near-bed flow motions that are possible during the occurrence of individual impulse events. We note that during any individual impulse event the instantaneous streamwise velocity may exceed or not u_{mean} and likewise for the wall-normal component, w, compared to w_{mean}. The current characterization emphasizes the mean motion taken over the entire duration of each impulse event.

[34] The fraction of all impulse events falling in each quadrant is shown in Figure 12, while surface plots of the impulse magnitude, I_i, and lift, $\langle F_L \rangle_i$, on $\langle u \rangle_i'$-$\langle w \rangle_i'$ plane are shown in Figures 13a and 13b, respectively. The data from all uniform flow experiments are used for Figure 12, whereas run U3 was used in Figure 13.

[35] From Figure 12, it is clear that impulse events are almost exclusively associated with Q I and Q IV, and for the lowest u^* case (U9), they are exclusively associated with the first and fourth quadrant. The largest fraction appears in Q IV but more than 20% of all impulse events are associated with flow movement characterized by the first quadrant. This supports, in part and in the context of impulse, the conclusions drawn by *Heathershaw and Thorne* [1985] and *Nelson et al*. [1995] that positive streamwise fluctuations dominate sediment entrainment. We note that as the flow strength decreases (from run U1 to U9), the fraction of events occurring in the fourth quadrant increases. For the Re^* range spanning the present experiments, this increase is from 67% to 78% and is compensated by a reduction in the number of impulse events in

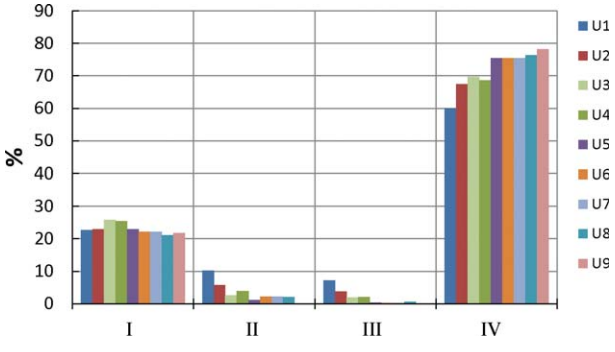

Figure 12. Bar plots of % total number of impulse events for each quadrant for all nine uniform flow runs.

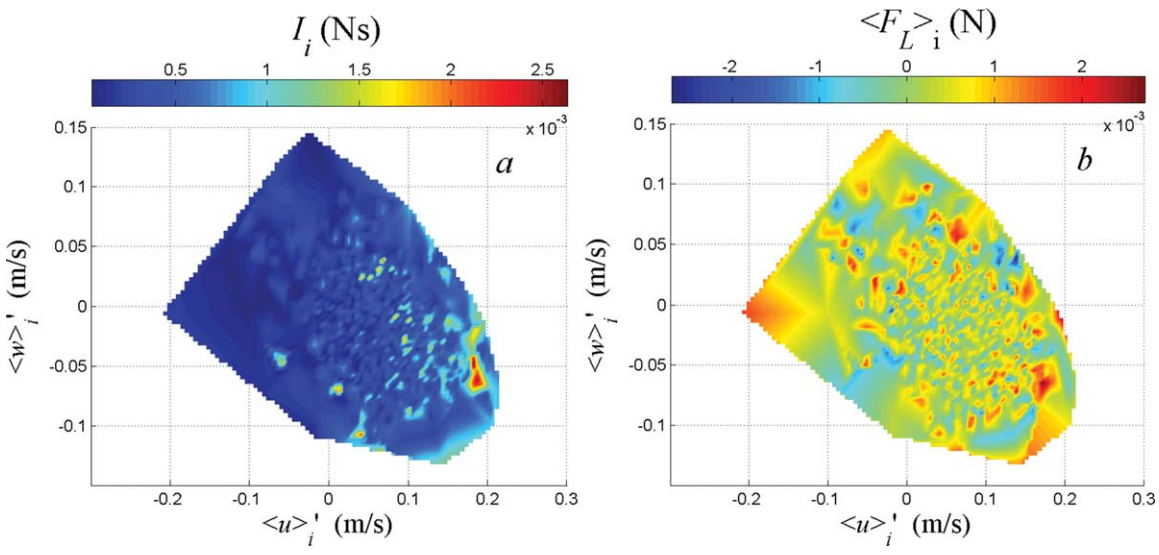

Figure 13. The 3-D surface plots of (a) impulse on $\langle u\rangle'$-$\langle w\rangle'$ plane. Color bar on top indicates the impulse magnitude. (b) Lift force associated with impulse events on $\langle u\rangle'$-$\langle w\rangle'$ plane. Color bar indicates the lift force magnitude/direction. Run U3.

both second and third quadrants from 10% to 0 and from 8% to 0, respectively. The number of impulse events observed in the first quadrant remains nearly constant, around 22% of the total number, for all runs. We emphasize that all events displayed in the figures correspond to events in which the force magnitude exceeds the critical value required to just initiate motion (but not necessarily fully dislodge the grain).

[36] Figures 13a and 13b display the magnitude of the impulse and lift events in the quadrant plane. From Figure 13a, it is apparent that the largest magnitude impulses occur in Q I and Q IV, with the most extreme events occurring in the fourth quadrant. These latter extreme impulse levels are however rare, (see e.g., Figure 4b). Lift force associated with impulse events are shown on the quadrant plane in Figure 13b. Again, it is observed that positive lift forces associated with the impulse events dominate in Q I and Q IV with no clear preference (in terms of magnitude) for either quadrant. The dominance of Q I and Q IV for both impulse and lift suggest a close connection between the streamwise fluctuations, drag and lift. This is consistent with the results of *Celik* [2011], where a strong positive correlation between u and drag is measured along with a strong positive correlation between drag and lift fluctuations. We also note that the average lift force taken over all impulse events is positive and a few percent of the submerged weight of the grain, while fluctuations in the lift about the mean can reach up to 20% of the submerged weight (Figure 10b). This is true for all of the uniform flow experiments. The influence of lift force on particle dislodgment will be discussed in greater detail in the next section.

4.3. Implications for Particle Entrainment

4.3.1. Effect of Lift Force on the Critical Impulse

[37] The rare extreme impulse events described by various combinations of T_i, and $\langle F_D\rangle_i$ are expected to dislodge the grain from its pocket when they exceed a critical impulse level, I_{cr}. When the influence of lift force is negligible, the critical drag force needed to initiate motion, F_{Dcr}, is constant (for a given local pocket geometry), and the corresponding I_{cr} value is also fixed and can be determined through energy considerations [*Diplas et al*., 2008; *Celik et al*., 2010]. However, as suggested by *Smart and Habersack* [2007], *Detert et al*. [2010], and *Celik* [2011], lift force fluctuations are not always negligible and so may affect the critical force necessary to initiate motion and thus the critical impulse to fully dislodge the grain. That is, the fluctuating lift force will increase or decrease the effective submerged weight of the grain and thus the resistance force. It is possible to incorporate the lift force associated with individual impulse events, $\langle F_L\rangle_i$, in calculating an effective particle weight, and consequently, a varying critical impulse value, I_{cr}, which is a function of W_s, Δz, and $\langle F_L\rangle_i$ for each flow event, where Δz is the vertical displacement of the grain during its dislodgment. The technique is discussed in more detail in *Celik et al*. [2010] but for another purpose.

[38] In order to demonstrate the influence of the event-based lift force on the critical impulse values, a 2-D (joint) histogram of impulse versus lift force is shown in Figure 14 (using data from run U2). In Figure 14, the demarcation line specifying the critical impulse necessary to cause full grain dislodgment is indicated with a solid line. If the lift force is neglected the vertical line represents I_{cr}. Events in Figure 14 which fall to the right of this line exceed I_{cr} and according to the impulse criterion will necessarily result in full dislodgment of the mobile Teflon grain, for the conditions of these tests. Events to the left of the line carry insufficient impulse to remove the grain from its pocket. If the fluctuating event-based lift force is included, the demarcation line for I_{cr} is rotated as shown in Figure 14. For positive lift fluctuations, the critical impulse is reduced while negative lift increases the effective submerged weight and so the critical level.

[39] The effect of fluctuating lift during impulse events is significant. Data from run U2 in Figure 14 shows that the

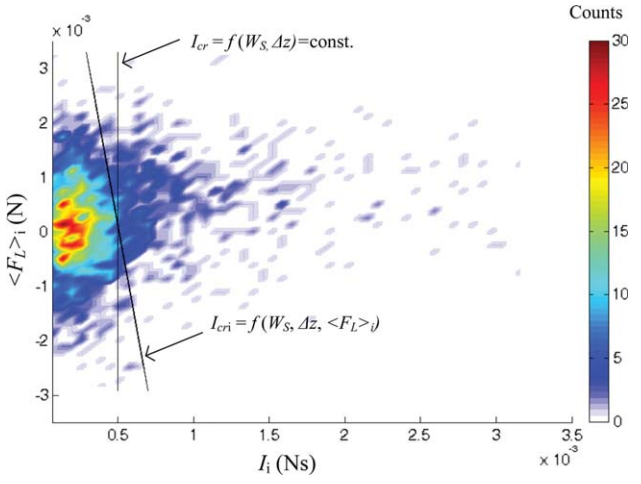

Figure 14. Surface plot of the 2-D histogram of impulse versus lift force (from run U2–2522 impulse events were used, number of bins: 50 × 50 on I-$\langle F_L \rangle$ plane). Color bar indicates the counts. This data in Figure 14 is the same as in Figure 15b.

number of events above the actual critical impulse (obtained by accounting for the positive lift contribution) is 333. However, if a constant critical impulse value is used (by neglecting the lift contribution), then the number of events above this fixed level is found to be 280. That is, false negatives account for 19% of the events determined by assuming a constant critical impulse value. False positives, which are above the constant critical impulse value but still below the actual impulse value (obtained by accounting for the negative lift contribution), are nearly 2%. Therefore, neglecting the influence of lift force causes a net 17% underestimation in the number of events that are in fact capable of causing particle entrainment. This helps to explain the existence of false positives and false negatives in the results of *Diplas et al*. [2008] (Figure 4c), where the effect of lift was neglected. It is noted that the fraction of false events discussed here for the U2 run is representative of the numbers obtained in the other uniform flow runs. Therefore, it is concluded that the fluctuations in lift force, even for a fully exposed particle, do play a significant role in particle dislodgment.

4.3.2. Number of Detected Impulse Events

[40] The hypersensitivity of bedload transport to the applied wall stress for conditions below or near the threshold of motion is well documented. In *Celik et al*. [2010], it was demonstrated that the impulse criterion for grain entrainment captures a comparable hypersensitivity of the number of impulses above to $F_{D\mathrm{cr}}$. In that investigation, which did not use measured surface pressures, $F_{D\mathrm{cr}}$ was artificially adjusted by ±25% to expose this extraordinary sensitivity to the threshold force. Here, the threshold force is constant, but the applied bed stress varies by ∼20% (increasing from U9 to U1). In Figure 15, the computed number of impulse events per unit time, n (see Table 1), based upon actual measured pressure differences (with $F_D \geq F_{D\mathrm{cr}}$) and using equations (1) and (2), is plotted as a function of Reynolds number based upon u^*, Re^*. As Re^* increases from 330 to 438, the number of impulse events increases from 11/min (0.18/s) to 230/min (3.8/s). Linear regression on the data reveals a power law with an exponent on Re^* of 10.6. Since the force imparted by individual impulse events does not vary dramatically from event to event (Figure 10a), and the mean applied wall stress, ρu^{*2}, varies only modestly between these experiments, this high sensitivity is associated with the temporal characteristics of the near wall turbulence, and the statistical behavior of these temporal features.

4.3.3. Cylinder Wake Flow and the Effect of Turbulence Intensity

[41] *Sumer et al*. [2003] conducted flume experiments with a sand bed in the wake of a cylinder and concluded that the sediment transport increased significantly with increasing turbulence intensity. *Nelson et al*. [1995] made similar observations in the wake of a backward facing step. Here, using the instrumented grain with surface pressure taps, as well as the mobile grain setup, a set of experiments were performed, similar in character to Sumer et al., in which a circular cylinder was mounted horizontally across the flume width upstream of the target grain. The purpose of these tests was to ascertain the influence (through the measured entrainment rates of the mobile grain and measured instantaneous forces on the instrumented grain) of the wake-flow field on an exposed grain. That is, how does the increased turbulence intensity induced by the cylinder manifest itself in the grain forces and its entrainment? Is the turbulence intensity a surrogate for a more fundamental underlying physical effect on the grain? These experiments are preliminary, and we present only a very limited number of results; specifically, the effect of turbulence intensity on the number of impulse events. Some features of the cylinder flows have been presented briefly in previous sections, e.g., when discussing the impulse probability distributions and force characteristics.

[42] As shown in Table 1, a 50% increase in the turbulence intensity near the grain due to the presence of a cylinder resulted in a sixfold increase in the particle entrainment frequency, n_e. The entrainment frequency is measured using the nonintrusive, laser-based grain motion instrumentation system. With this system full grain dislodgments are detected using the continuous output of the photodetector [*Diplas et al*., 2010]. Overall, the available data from the cylinder tests show that the particle entrainment frequency increases with about the fourth power of the turbulence intensity, Figure 16. It is recalled that for the uniform flow experiments, without a cylinder present, the grain experiences a small positive average lift force of a few percent of its submerged weight, with fluctuations of up to ±30%, thus reducing the effective submerged weight of the grain, and so enhancing the likelihood of entrainment. The pressure measurements on the instrumented grain with a cylinder mounted upstream reveals that the average lift force experienced by the exposed grain increases when compared to the uniform flow tests, reducing the effective particle weight by up to 30%, and that the fluctuating force about the mean can reach as high as 80% of the submerged weight [*Celik*, 2011]. It was shown by *Celik et al*. [2010] that an artificial decrease in the particle density by 25% causes nearly an order of magnitude increase in the number of impulse

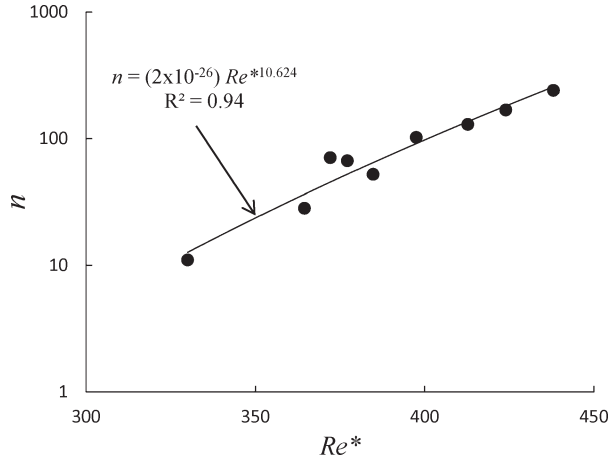

Figure 15. Plot of the total number of impulse events per min versus Re^*. Line describes the overall variation of n calculated from directly measured F_D data with Re^* ($R^2 = 0.94$).

events capable of entraining the particle. Despite the variability in flow and bed material parameters when comparing these experiments to Sumer, this behavior shows strong qualitative similarities to those reported by them, as shown in Figure 16. Here, the bedload transport rate, q, and the particle entrainment frequency are compared, in which both parameters are nondimensionalized by their counterparts from undisturbed flow conditions. Note that, *Sumer et al*. [2003] kept the bed shear stress constant while generating external turbulence by use of a cylinder to isolate the effect of turbulence level in their flume tests. In our experiments, the flow was not adjusted in the cylinder wake tests. Instead, the bed shear stress upstream was kept the same as in the undisturbed flow experiments, UC in Table 1. The observed similarity here in the trends (see the exponents shown in the inset of Figure 16) nevertheless helps explain the phenomenon observed by *Sumer et al*. [2003].

[43] We conclude from these preliminary tests that in the case of the cylinder wake, the increased entrainment rate is the result of a combination of an increase in the number of impulse events above critical as a result of the dramatically increased lift in the cylinder wake and an increase in the rate of impulses per unit time (associated with the increase in turbulence intensity).

5. Discussion and Conclusions

[44] We investigated the previously proposed impulse concept more rigorously using directly measured surface pressures acting on a spherical grain under both uniform and unsteady cylinder wake flows. These measurements provide a more complete and reliable time history of the fluctuating pressures applied upon the grain The number of impulse events per minute determined from these experiments when the hydrodynamic force applied on the test grain exceeded a critical value increases very rapidly and consistently, by more than an order of magnitude (20-fold), over a modest (33%) change of roughness Reynolds number. These impulse events are well represented by a log-normal pdf or a similar long-tail distribution. Both of these findings are in good agreement with those obtained from similar experiments via indirect (velocity-based measurements obtained one diameter upstream of a grain and along its centerline via an LDV) impulse calculations reported in *Celik et al*. [2010]. This result justifies the use of velocity measurements to determine the instantaneous hydrodynamic force record applied upon a grain or other flow obstruction and from that calculate the content of the associated impulse events. Though this approach requires significant resources, it is much easier to employ in the field and laboratory experiments compared to the other potentially more accurate but far more demanding, and at times an impractical option of obtaining direct pressure fluctuation measurements. This type of detailed hydrodynamic description of the flow is of paramount importance if we are to improve the tools currently available for modeling

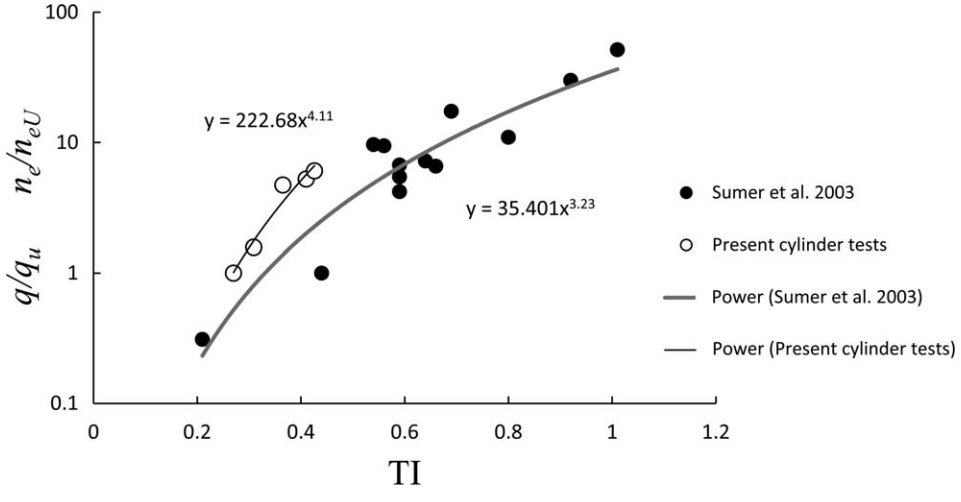

Figure 16. Ratios of bed material movement (bed load, q, data from *Sumer et al*. [2003], particle entrainment frequency, n_e, data from present tests) obtained in cylinder test to that of undisturbed flow conditions versus turbulence intensity.

grain erosion and a wide range of other engineering and geomorphological processes.

[45] The present results demonstrate the dominant role the local positive streamwise velocity fluctuations play on particle dislodgment. This is consistent with the traditional understanding about the mechanism responsible for lift and drag forces, generalized here to corresponding instantaneous values. Furthermore, our findings indicate that the vast majority of the significant impulse events that lead to grain movement occur during first (outward interaction) and fourth (sweep) quadrant flow episodes.

[46] The occurrence of instantaneous lift forces does not exhibit any preference in terms of sign (positive or negative) when the applied drag forces are modestly above the critical value, $F_{D\mathrm{cr}}$. However, in the presence of flow events associated with considerably stronger drag forces and impulse content exceeding the critical value, I_{cr}, lift force incidents, though not very frequent, tend to be positive and of higher magnitude. In the latter case, these coincident lift forces can have a significant destabilizing effect on particle mobility.

[47] Finally, it was concluded that the major increase in the entrainment rate of particles located in the wake of a flow obstruction can be attributed to two collaborating mechanisms, significantly enhanced lift and increased turbulence intensity.

Notation

δ impulse intensity (coefficient of variation of impulse).
Δx detectable level of displacement in the streamwise direction.
Δz detectable level of displacement in the vertical direction.
ν kinematic viscosity.
A projected area of the spherical test grain.
C_D drag coefficient.
$\langle C_D \rangle$ average drag coefficient over impulse event duration.
$\langle C_D \rangle_{\mathrm{mean}}$ ensemble average of $\langle C_D \rangle$.
d grain diameter.
D pipe diameter.
e the distance between the bed and the bottom of the cylinder.
f_V hydrodynamic mass coefficient.
F_D drag force.
$\langle F_D \rangle$ time-average drag force over the duration of an impulse event.
$\langle F_D \rangle_{\mathrm{mean}}$ ensemble average of $\langle F_D \rangle$.
$F_{D\mathrm{cr}}$ critical drag force.
F_L lift force.
$F_{L\mathrm{mean}}$ time-average lift force over the entire sampling duration.
$\langle F_L \rangle$ time-average lift force over the duration of an impulse event.
$\langle F_L \rangle_{\mathrm{mean}}$ ensemble average of $\langle F_L \rangle$.
g gravitational acceleration.
I impulse magnitude.
$\hat{I}$ dimensionless impulse.
I_{cr} critical impulse.
I_{cri} critical impulse for the ith event.
I_{mean} time-average impulse over the entire sampling duration.
I_{std} standard deviation of impulse.
L distance between the center of the instrumented test grain and centerline of the cylinder.
m mass of the grain.
n total number of flow induced impulse events per unit time.
n_e total number of grain entrainment events per unit time.
n_{eU} total number of grain entrainment events per unit time for undisturbed flow conditions.
p_1 pressure at the front of the particle.
p_2 pressure at the back of the particle.
p_3 pressure at the top of the particle.
p_4 pressure at the bottom of the particle.
q bed load.
q_u bed load transport for undisturbed flow conditions.
Re^* roughness Reynolds number.
T impulse and force duration.
TI turbulence intensity.
u streamwise velocity component.
u_{mean} time-average streamwise velocity component over the entire sampling duration.
$\langle u \rangle$ time-average streamwise velocity component over impulse event duration.
$\langle u \rangle_{\mathrm{mean}}$ ensemble average over all $\langle u \rangle$.
$\langle u \rangle'$ fluctuations of time-average streamwise velocity component over impulse event duration.
u^* friction velocity.
w vertical velocity component.
w_{mean} time-average vertical velocity component over the entire sampling duration.
$\langle w \rangle$ time-average vertical velocity component over impulse duration.
$\langle w \rangle'$ fluctuations of time-average vertical velocity component over impulse event duration.
V_{init} theoretical initial velocity of the particle in the streamwise direction.
W_S weight of the submerged particle.
x streamwise axis.
X lever arm aligned with bed.
y spanwise axis.
z vertical axis.
Z lever arm normal to bed.

[48] **Acknowledgments.** The support of the National Science Foundation (grants EAR-0439663, EAR-0738759, and CBET-1033196) and the Army Research Office is gratefully acknowledged.

References

Balakrishnan, M. (1997), The role of turbulence on the entrainment of a single sphere and the effects of roughness on fluid-solid interaction, Ph.D. dissertation, Mech. Eng. Dep., Va. Polytech. Inst. and State Univ., Blacksburg.

Cameron, S. M. (2006), Near-boundary flow structure and particle entrainment, Ph.D. dissertation, Univ. of Auckland, New Zealand.

Celik, A. O. (2011), Experimental investigation of the role of turbulence fluctuations on incipient motion of sediment, Ph.D. dissertation, Civil

and Environ. Eng. Dep., Va. Polytechnic Inst. and State Univ., Blacksburg.

Celik, A. O., P. Diplas, C. L. Dancey, and M. Valyrakis (2010), Impulse and particle dislodgement under turbulent flow conditions, *Phys. Fluids*, *22*, 046601:1–13, doi:10.1063/1.3385433.

Coleman, N. (1967), *A theoretical and experimental study of drag and lift forces acting on a sphere resting on a hypothetical streambed, paper presented at the 12th Congress of the International Association of Hydraulic Research*, IAHS, Fort Collins, Colo.

Detert, M., V. Weitbrecht, and G. H. Jirka (2010), Laboratory measurements on turbulent pressure fluctuations in and above gravel beds, *J. Hydraul. Eng.*, *136*(10), 779–789.

Diplas P., C. L. Dancey, A. O. Celik, M. Valyrakis, K. Greer, and T. Akar (2008), The role of impulse on the initiation of particle movement under turbulent flow conditions, *Science*, *322*, 717–720.

Diplas, P., A. O. Celik, C. L. Dancey, and M. Valyrakis. (2010), Non-intrusive method for detecting particle movement characteristics near threshold flow conditions, *J. Irrig. Drain. Eng.*, *136*(11), 774–780.

Dwivedi, A., B. Melville, and A. Y. Shamseldin (2010), Hydrodynamic forces generated on a spherical sediment particle during entrainment, *J. Hydraul. Eng.*, *136*(10), 756–769.

Dwivedi, A., B., Melville, A.Y., Shamseldin, and T. K. Guha (2011a), Flow structures and hydrodynamic force during sediment entrainment, *Water Resour. Res.*, *47*, W01509, doi:10.1029/2010WR009089.

Dwivedi, A., B., Melville, A. Y. Shamseldin, and T. K. Guha (2011b), Analysis of hydrodynamic lift on a bed sediment particle, *J. Geophys. Res.*, *116*, F02015, doi:10.1029/2009JF001584.

Einstein, H. A., and E. A. El-Samni (1949), Hydrodynamic forces on a rough wall, *Rev. Mod. Phys.*, *21*(3), 520–524.

Fenton, J. D. and J. E. Abbot (1977), Initial movement of grains on a stream bed : The effect of relative protrusion, *Proc. R. Soc. London A*, *352*, 523–537.

Gessler, J. (1971), *Beginning and ceasing of sediment motion, in River Mechanics*, edited by H. W. Shen, chap. *7*, Water Resour. Publ., Forth Collins, Colo.

Grass, A. J. (1970), Initial instability of fine bed sand, *J. Hydraul. Div. Am. Soc. Civ. Eng.*, *96*(3), 619–632.

Heathershaw, A. D., and P. D. Thorne (1985), Sea-bed noises reveal role of turbulent bursting phenomenon in sediment transport by tidal currents, *Nature*, *316*, 339–342, doi:10.1038/316339a0.

Hofland, B., R. Booij, and J. Battjes (2005), Measurement of fluctuating pressures on coarse bed material, *J. Hydraul. Eng.*, *131*(9), 770–781.

Jackson, R.G. (1976), Sedimentological and fluid-dynamic implications of the turbulent bursting phenomenon in geophysical flows, *J. Fluid Mech.*, *77*, 531–560.

Nelson, J. M., R. L. Shreve, S. R. MacLean, and T. G. Drake (1995), Role of near-bed turbulence structure in bed load transport and bed form mechanics, *Water Resour. Res.*, *31*(8), 2071–2086.

Papanicolaou, A. N., P. Diplas, N. Evaggelopoulos, and S. Fotopoulos (2002), Stochastic incipient motion criterion for spheres under various bed packing conditions, *J. Hydraul. Eng.*, *128*(4), 369–380.

Radspinner, R., P. Diplas, A. Lightbody, and F. Sotiropoulos (2010), River training and ecological enhancement using in-stream structures, *J. Hydraul. Eng.*, *136*(12), 967–980.

Schmeeckle, M. W., J. M. Nelson, and R. L. Shreve (2007), Forces on stationary particles in near-bed turbulent flows, *J. Geophys. Res.*, *112*, F02003, doi:10.1029/2006JF000536.

Sumer B. M., and E. J. Fredsoe (2006), *Hydrodynamics Around Cylindrical Structures*, World Scientific, Singapore.

Smart G. M., and H. M. Habersack (2007), Pressure fluctuations and gravel entrainment in rivers, *J. Hydraul. Res.*, *45*(5), 661–673.

Sumer, B. M., L. H. C. Chua, N. S. Cheng, and J. Fredsoe (2003), Influence of turbulence on bed load sediment transport, *J. Hydraul. Eng.*, *129*(8), 585–596.

Sutherland, A. J. (1967), Proposed mechanism for sediment entrainment by turbulent flows, *J. Geophys. Res.*, *72*(24), 6183–6194.

Valyrakis, M., P., Diplas, C. L., Dancey, K., Greer, and A. O. Celik (2010), Role of instantaneous force magnitude and duration on particle entrainment, *J. Geophys. Res.*, *115*, F02006, doi:10.1029/2008JF001247.

Valyrakis, M., P., Diplas, and C. L. Dancey (2011), Entrainment of coarse grains in turbulent flows: An extreme value theory approach, *Water Resour. Res.*, *47*, W09512, doi:10.1029/2010WR010236.

White, C. R. (1940), The equilibrium of grains on the bed of a stream, *Proc. R. Soc. London A*, *174*, 322–338.

Wiberg, P. L., and J. D. Smith (1987), Calculations of the critical shear stress for motion of uniform and heterogeneous sediments, *Water Resour. Res.*, *23*, 1471 – 1480, doi:10.1029/WR023i008p01471.

Wu, F. C., and Y. J. Chou (2003), Rolling and lifting probabilities for sediment entrainment, *J. Hydraul. Eng.*, *129*(2), 110–119.

Zanke, U. C. E. (2003), On the influence of turbulence on the initiation of sediment motion, *Int. J. Sediment Res.*, *18*(1), 17–31.